

Article

Dynamic Response of Outer Windshield Structure in Different Schemes under Aerodynamic Load

Ming-Zan Tang^{1,2,3}, Xiao-Hui Xiong^{1,2,3}, Xiao-Bai Li^{1,2,3,*}, Guang Chen^{1,2,3}, Jie Zhang^{1,2,3}, Mu Zhong^{1,2,3} and Bo Sun^{1,2,3}

¹ Key Laboratory of Traffic Safety on Track, Central South University, Ministry of Education, Changsha 410075, China

² Joint International Research Laboratory of Key Technology for Rail Traffic Safety, Changsha 410075, China

³ National & Local Joint Engineering Research Centre of Safety Technology for Rail Vehicle, Changsha 410075, China

* Correspondence: gszxlb@163.com; Tel.: +86-731-82656673

Abstract: With the increase in high-speed train (HST) operation speed, the light-weight design of the train body and component structure is pursued to reduce energy consumption during operation, but this seriously deteriorates the aerodynamic performance of the light-weight structure outside the train body under the effect of strong unsteady airflow, and the more obvious case is the frequently occurring problem of vibration, large deformation, and damage to the rubber exterior windshield at the connection position of HST carriages. We investigate the fluid–structure coupling mechanism of the interaction between the rubber external windshield and aerodynamic force, and compare the dynamic characteristics of windshield structure under different design parameters. A numerical simulation of three rubber outer windshield structure parameters (sidewall distance of U-shaped capsule, sidewall thickness, sidewall inclination angle) is carried out using FSI simulation of the two-way coupling method. The aerodynamic load, airflow dynamics around the windshield, and the nonlinear vibration and deformation form of the windshield is analyzed in detail. The results show that the aerodynamic response of the HST rubber external windshield analyzed by the FSI method is in good agreement with the full-scale test results. Additionally, the stiffness of the windshield can be improved by increasing the thickness of the windshield sidewall. When the distance between the sidewall of the windshield is increased, an insufficient thickness at the top of the arc causes a large local deformation at the top of the arc of the windshield. The method established and relevant research results can provide good support for the aerodynamic stability evaluation of HST windshields.

Keywords: fluid–structure interaction; nonlinear vibration; deformation form; structural design; high-speed train



Citation: Tang, M.-Z.; Xiong, X.-H.; Li, X.-B.; Chen, G.; Zhang, J.; Zhong, M.; Sun, B. Dynamic Response of Outer Windshield Structure in Different Schemes under Aerodynamic Load. *Appl. Sci.* **2023**, *13*, 3879. <https://doi.org/10.3390/app13063879>

Academic Editor: Hassan Hemida

Received: 29 January 2023

Revised: 7 March 2023

Accepted: 15 March 2023

Published: 18 March 2023



Copyright: © 2023 by the authors. Licensee MDPI, Basel, Switzerland. This article is an open access article distributed under the terms and conditions of the Creative Commons Attribution (CC BY) license (<https://creativecommons.org/licenses/by/4.0/>).

1. Introduction

With the continuous improvement in the speed of passenger train operation, the fluid drag force acting on the train body increases significantly, leading to more energy consumption [1–3]. A smooth design of the HST body surface is important for setting the exterior windshield at the connection between train carriages, which can effectively reduce the aerodynamic resistance and aerodynamic noise of the connecting parts of vehicles [4–6], and reduce the energy consumption of the train operation. When the train passes through a curve, the distance between the adjacent carriages changes. The outer windshield of the carriage end is usually made of rubber material with certain elasticity and stiffness, or a certain gap is reserved for the outer windshield, which provides a safe offset distance for the relative movement of the train carriage. Owing to its good curve passing ability and drag and noise reduction characteristics, the windshield is widely used in HSTs, as shown in Figure 1.

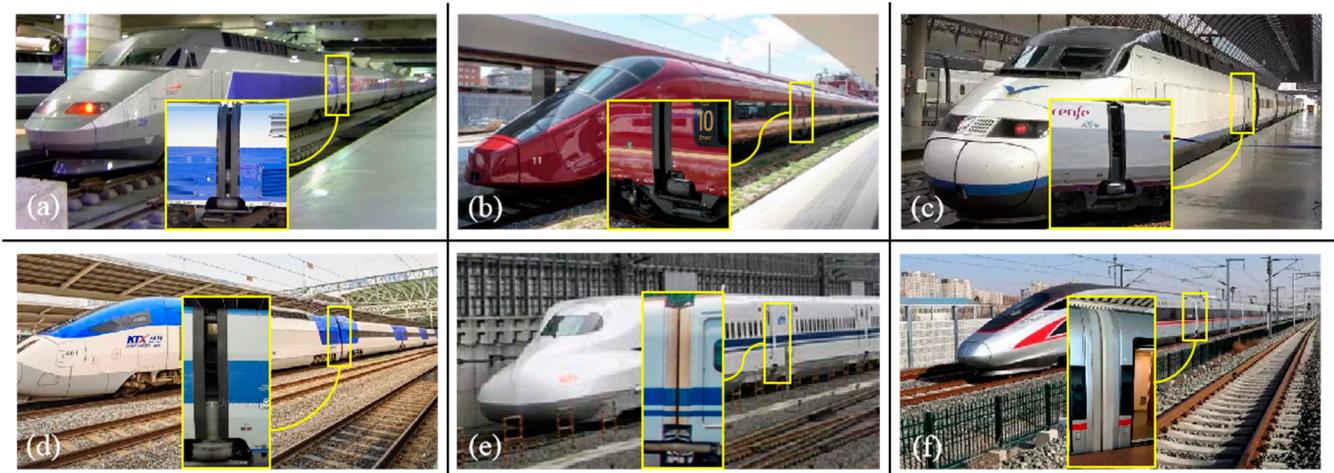


Figure 1. HSTs having various outer windshield configurations: (a) TGV in France, (b) AGV in Italy, (c) AVE in Spain, (d) KTX2 in Korea, (e) N700 in Japan, (f) CR400 in China.

It is known that the airflow around the HST is within a turbulent state when the train runs at high speed, especially at the connection between carriages [7–10]. The flow separation produces a great quantity of vortices, and the movement and development of the vortices at the end of the carriage leads to the external windshield being subjected to complex and strong aerodynamic load [11–13]. Owing to the stiffness and strength of rubber, which is much lower than that of metal materials, under the action of strong pulsating airflow around the connection of HST carriages, large deformation, vibration, and damage of the rubber outer windshield structure frequently occurs [14,15], seriously affecting the train running stability and reducing driving safety.

At present, research on HST windshields mainly focuses on aerodynamic drag, aerodynamic noise, and surrounding flow-field structure of the external windshield, and little work is focused on the FSI characteristics between the external windshield and the complex aerodynamic loads. Niu et al. [16] studied the aerodynamic performance of an exterior HST windshield at the running speed of 350 km/h and compared the effect of different schemes of the exterior windshield structure on the aerodynamic resistance of the train by full-scale testing and numerical simulation. Xia et al. [17], through the numerical simulation of one-eighth-scale HST models with different gap spacing between adjacent vehicles, found that different external windshield gaps have significant effects on the airflow structure and aerodynamic drag of train models. Noh et al. [18] researched the gangway noise of the carriage connection, and noise mitigation methods were suggested. It was found that the additional fairings structure blocked the influx of air in the carriage connection gap, and noise in the cavity was reduced by 8 ~ 10 dB at 300 km/h. Horiuchi [15] introduced that installing a full circumference hood between the carriage of FASTECH series trains can effectively suppress aerodynamic noise that occurs in the spaces between railcars. The relaxation state of the rubber exterior windshield, however, changes with train operation speed. Dai et al. [4] adopted a hybrid method to study the aerodynamic noise around the windshield region between carriages, and the results show that a full-windshield form is better for noise reduction, which apparently reduces the overall sound pressure level on the near-field sides. Cheng et al. [19] utilized the improved delayed–detached eddy simulation (IDDES) to resolve the flow field around the outer windshield by using different installation gaps (10, 20, and 30 mm). The aerodynamic forces on different windshield components, turbulent flow fields around the train-end area, and the corresponding low-dimensional modes were analyzed.

However, in previous research on the aerodynamic performance of HST external windshields, the external windshield structure is usually regarded as a rigid body, and the coupling effect between the elastic rubber structure and unsteady flow is not considered.

Jiang et al. [20], however, adopted the coupling scheme of computational fluid dynamics (CFD) and computational structural dynamics (CSD) to simulate the flutter problems of the outer windshield, and studied the CFD/CSD coupling simulation between the aerodynamic load and the first thirty order modes of the elastic outer windshield under eight different train speed conditions. The results provided the critical stable state of outer windshield vibration at different speed conditions. This method mainly considers the relationship between eigenfrequency and the flutter boundary, but fails to include the transient response recurrence for the windshield under aerodynamic load, the dynamic response characteristics of the interaction between the airflow around the carriage ends, and the external windshield structure.

When the train runs at a high speed, the aerodynamic pressure may cause deformation of the rubber windshield and induces vibration response of the windshield under vortex excitation. In turn, the vibration state and deformation of the exterior windshield affect the airflow movement around the connection region between carriages, changing the size and distribution of the aerodynamic load and affecting the frequency of vortex movement [14]. Additionally, the aerodynamic pressure distribution characteristics of the windshield can be affected by the geometric features of the windshield, and the material distribution of the windshield section can affect its structural stiffness and natural frequency. In view of the complex aerodynamic excitation characteristics and FSI behavior of the external windshield at the connection region between HST carriages, it is very difficult to study the aerodynamic stability and structural reliability of the HST windshield under strong aerodynamic loads.

Therefore, this paper studies the nonlinear vibration characteristics of the rubber windshield structure under the aerodynamic load action by using the two-way coupling FSI simulation method for three external windshield structures with different geometric shapes and structural sections. Additionally, the FSI behavior and causes for vibration related to the rubber external windshield are analyzed. The transient response and deformation characteristics for three different schemes of external windshield structure under the excitation of an unsteady flow field are compared, and the stress concentration positions of the different schemes of the rubber external windshield structure in the vibration response process are obtained. The research results can provide reference for aerodynamic stability analysis and optimization design of external HST windshields.

2. Methodology of Simulation

2.1. Numerical Method of FSI

According to the research on the FSI problem, the direct coupling method and region-dividing coupling method are commonly used to analyze FSI problems [21–23], which directly solve the coupling equations. In a grid system, the direct coupling method can use a format to promote the solution synchronously. However, for the highly nonlinear characteristics of FSI problems, the direct solution of the coupling equations requires more computing resources [24]. The region-dividing coupling method uses different solvers to calculate the respective physical variables, among which the common variables are updated by asynchronous transmission. Therefore, the procedures and methods of CSD and CFD can be fully utilized to maximize the independence of calculation between the solid domain and the fluid domain. Compared with the direct-coupling FSI method, it can greatly simplify the calculation. In this paper, the two-way, region-dividing coupling method is used to simulate the aerodynamic response of the rubber external HST windshield structure.

2.1.1. Governing Equations of Fluid Flows

Considering that the train running speed grade calculated by the numerical method is 350 km/h ($Ma < 0.3$), the compressibility of fluid is not considered. In addition, the airflow around the train has a high Reynolds number and is in a turbulent state. In the FSI calculation, the three-dimensional unsteady incompressible Reynolds average Navier–Stokes (RANS) method is used to calculate the flow field. The basic equations describing

fluid motion consist of the continuity equation and the Navier–Stokes equation. The equations for the mean velocity components \bar{u}_i and pressure (\bar{p}) are summarized as:

$$\frac{\partial \bar{u}_i}{\partial x_i} = 0 \tag{1}$$

$$\frac{\partial \bar{u}_i}{\partial t} + \bar{u}_j \frac{\partial \bar{u}_i}{\partial x_j} = -\frac{1}{\rho} \frac{\partial \bar{P}}{\partial x_i} + \frac{\partial}{\partial x_j} \left(v \frac{\partial \bar{u}_i}{\partial x_j} \right) + \frac{1}{\rho} \frac{\partial \tau_{ij}}{\partial x_i} \tag{2}$$

where x_i is the coordinate component in the Cartesian coordinate system in the direction of x, y, z ; \bar{u}_i is the mean velocity components of the air flow around the train in the direction of x, y, z ; \bar{P} is the average pressure; ρ is the density of air and is constant; τ_{ij} is the Reynolds stress tensor, which cannot formally be expressed in terms of mean flow variables. The usual way is to require the mean flow gradient together with a spatially varying turbulent viscosity based on local turbulent time/velocity and length scales to approximate the Reynolds stress. In this FSI simulation study of the HST rubber outer windshield, a more sophisticated two-equation shear stress transport (SST) $k - \omega$ model is utilized for the turbulence calculation model [25–27].

2.1.2. Transient Dynamic Analysis of Structure

The fluid force calculated by the fluid field provides the external load for the transient dynamic analysis of the structure. Based on the unsteady fluid excitation, the transient dynamic analysis of the rubber external windshield of the HST is carried out. The motion equation of the solid field is summarized as [28]:

$$[M] \{ \ddot{d}(t) \} + [C] \{ \dot{d}(t) \} + [K] \{ d(t) \} = \{ F(t) \} \tag{3}$$

where $[C]$, $[M]$, and $[K]$ are the damping, mass, and stiffness matrices, respectively; $d(t)$ is the displacement at a certain time for a discrete point; and $F(t)$ is the fluid force at a certain time. As structural damping is an important parameter in transient dynamic analysis, and the Rayleigh damping factor is considered in this paper, the calculation formula for Rayleigh damping is as follows:

$$C = \alpha \cdot M + \beta \cdot K \tag{4}$$

The basic structural response at the discrete time points can be obtained through a fixed integration time step Δt . The formula for calculating velocity and acceleration at discrete points of the solid structure is as follows:

$$(\dot{u}_n) = \frac{1}{2\Delta t} (u_{n+1} - u_{n-1}) \tag{5}$$

$$(\ddot{u}_n) = \frac{1}{\Delta t^2} (u_{n+1} - u_n + u_{n-1}) \tag{6}$$

The displacement of each discrete node is obtained through the transient dynamics calculation, which provides input for the mesh deformation of the fluid field.

2.1.3. Dynamic and Kinematic Equations of FSI

The structural model is established on a Lagrangian coordinate system and the displacements are the primary unknowns; the fluid physics continuum is always analyzed using an Eulerian coordinate system. However, for FSI calculations, the CFD model must be based on an arbitrary Lagrangian–Eulerian (ALE) coordinate system since the fluid–structure interface is deformable. The fluid and solid equations were solved continuously and iteratively, and the dynamic and kinematic conditions of the interaction should be satisfied at the FSI interface [29].

The dynamic and kinematic conditions of the FSI interface can be expressed as

$$\underline{d}_f = \underline{d}_s \quad (7)$$

$$n \cdot \underline{\tau}_f = n \cdot \underline{\tau}_s \quad (8)$$

where \vec{d}_s and \vec{d}_f are, respectively, the displacement values of solid and fluid on the FSI interface, and $\vec{\tau}_s$ and $\vec{\tau}_f$ are, respectively, the stress values of solid and fluid on the FSI interface.

In the FSI calculation, the fluid velocity condition results from the kinematic condition, and the equation is as follows:

$$\dot{\underline{d}}_s = \underline{u} \quad (9)$$

In the unsteady-state analyses, the kinematic conditions in the solid model determine the position of the nodes in the FSI interface in the fluid domain, and then the governing equations of the fluid flow in the ALE formulations are solved.

On the other hand, in the fluid calculation domain, the fluid traction is integrated into fluid force along FSI interfaces and exerted onto the structure node of the solid model, and the equation is as follows:

$$\underline{E}(t) = \int h^d \underline{\tau}_f \cdot dS \quad (10)$$

where h^d is the virtual quantity of the solid displacement.

2.2. Geometric Model

The geometric model of the HST used for the FSI calculation of the rubber external windshield of the train is mainly composed of three carriages (head carriage, intermediate carriage, and tail carriage) and two sets of rubber exterior windshields. The geometric streamline characteristics and bogie structure of the train model are retained, while the pantograph, door, window, and other parts are simplified. To better compare the aerodynamic effects of the three external windshield structure schemes and reduce the calculation amount, the calculation model only changes the external windshield structure, and sets the outer windshield side as an FSI model. The geometric model used for the numerical calculation is shown in Figure 2a. Figure 2b shows the structural sections of the outer windshield in three different schemes, and the three calculation models are defined as Case1, Case2, and Case3. Compared with Case 1, the sidewall distance of the U-shaped capsule in Case 2 is increased by 40 mm, the sidewall thickness is increased by 5 mm, and the sidewall has a 5° inclination angle with the train surface.

Compared with Case 1, Case 3 increases the sidewall distance of the U-shaped capsule by 140 mm, the sidewall thickness by 2 mm, and the sidewall has a 5° inclination to the train surface. Because the influence of each variable parameter on the aerodynamic performance and dynamic characteristics of the rubber external windshield is not considered in detail when designing the windshield of the three schemes, the dynamic response and deformation form characteristics of the rubber external windshield are different in the application process. In this paper, through the FSI modeling of the three schemes of the external windshield structure, the approximate influence trend of the parameters on the aerodynamic response of the rubber exterior windshield can be obtained. In the future, this will be of great significance to the parametric design of rubber exterior windshield structures.

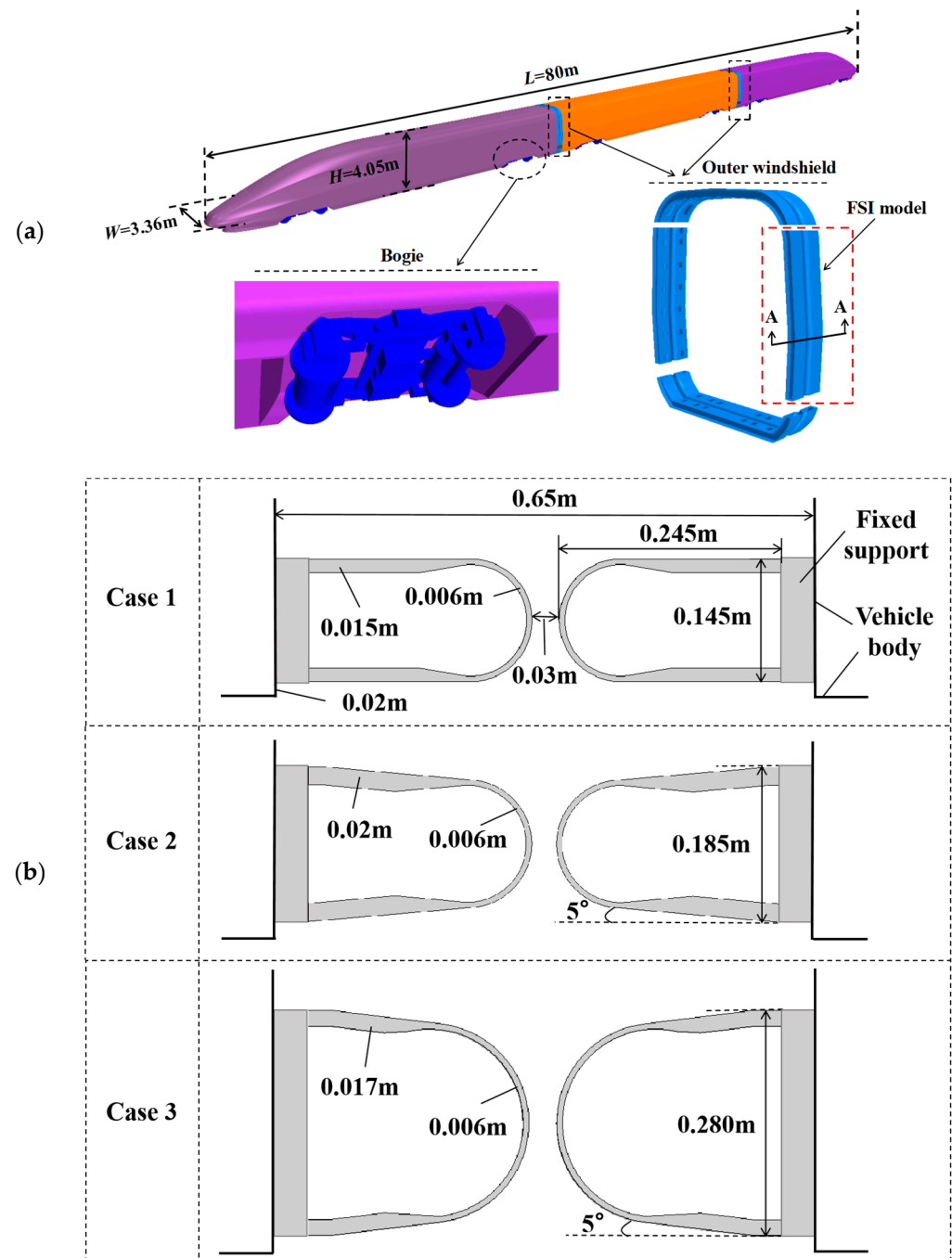


Figure 2. Computational model: (a) train model, (b) geometric outline at A–A section of different outer windshield schemes.

2.3. Computational Domain and Boundary Condition

In the FSI calculation, for reducing the influence of the fluid-domain boundary conditions on the airflow around the train, the height H (4.05 m) is defined as the characteristic dimension in this study; the length, width, and height are set to $60H$, $20H$, and $10H$, respectively. Additionally, the tip of the train nose is $10H$ away from the velocity inlet boundary, and the train is $0.05H$ above the ground. To ensure full development of the flow field at the rear of the train, the tip of the tail carriage is $30H$ away from the pressure outlet boundary [10,16]. Figure 3 shows the boundary conditions and calculation area for the FSI simulation. The wall of the side structure of the external windshield is set as an FSI interface. The relative wind-speed method is used to simulate the relative motion between the train

and airflow with given boundary conditions [30,31]. The uniform incoming flow velocity at the speed inlet boundary in front of the train is $V = -V_i$. To describe the characteristics of the incoming flow, the turbulent intensity of incoming flow in the calculation domain is 1% and the turbulent viscosity ratio is 10. Figure 3b shows the fluid–structure interface condition.

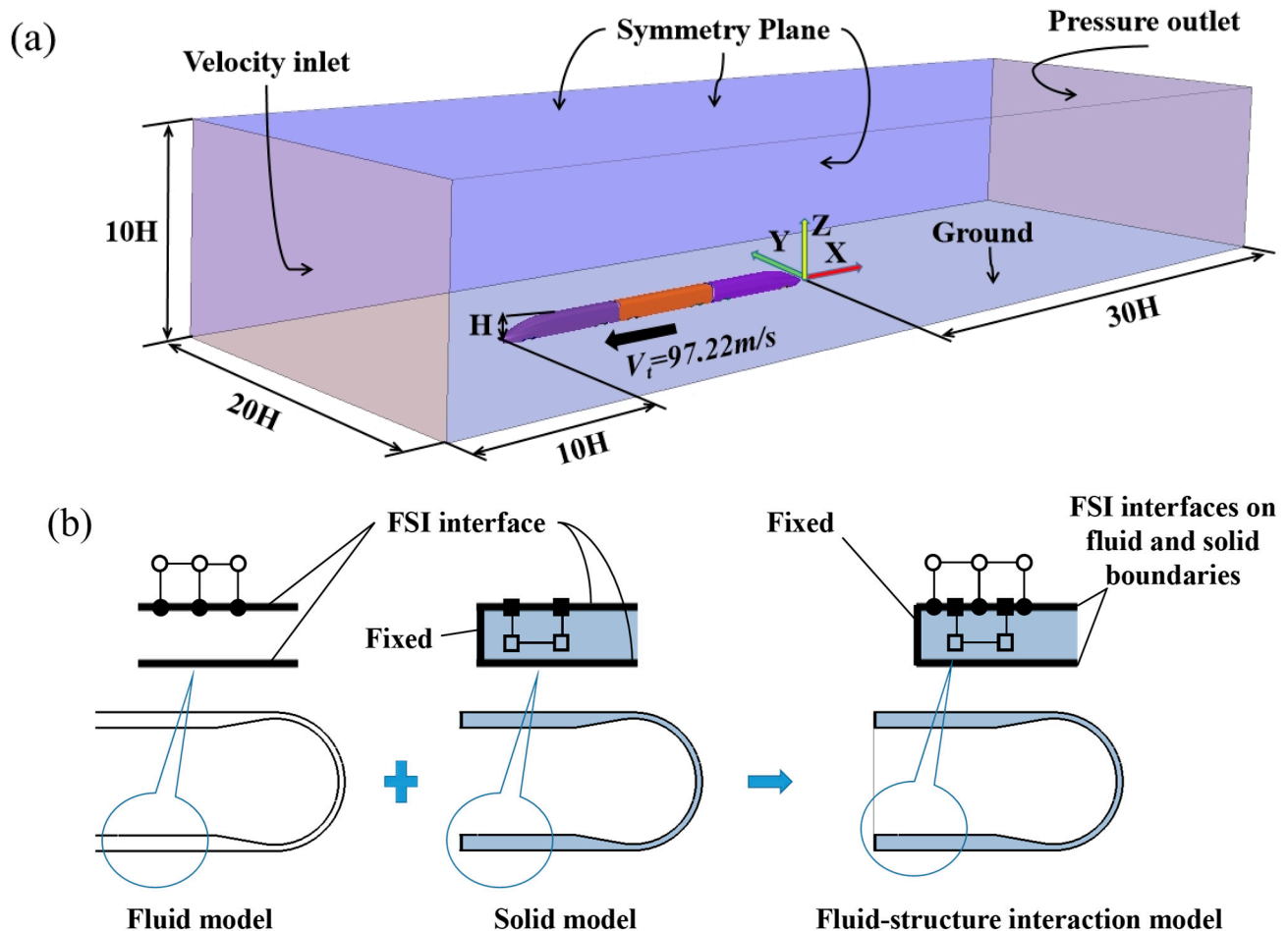


Figure 3. Boundary conditions and computational domain: (a) fluid model, (b) boundary conditions of FSI.

2.4. Meshing Strategy and Brief Description of the Solver

In order to reduce the influence of grid settings on the aerodynamic effect analysis of the outer windshield of different schemes, the grid settings are consistent for the calculation models of the outer windshield of the three schemes. The solid model and the fluid model were discretized using the elements that are available in the software Abaqus and STAR-CCM, respectively. Details of the computational grid used for the fluid model and the solid model are shown in Figure 4. Ten prism layers were applied at the wall of windshield and train model, with a total thickness of four millimeters [32,33]. As shown in Figure 4a, a refinement box was built around the full-scale train model, and the external windshield area for local mesh encryption. For the full-scale train model, the smallest mesh used on the outer windshield surface had a size of 4 mm, the y^+ around the train ranging from 0.1 to 10 [16,19]. To verify the accuracy of the grids and to avoid the influence of mesh resolution on the resulting analysis, a grid sensitivity test was performed for a train speed of 350 km/h [14,19].

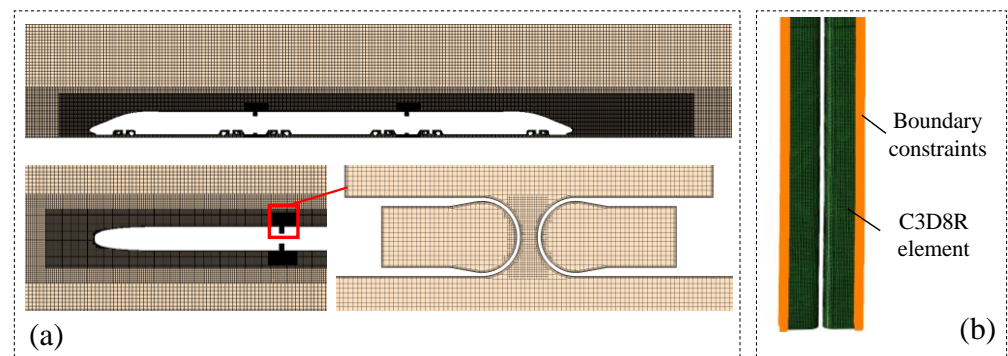


Figure 4. Mesh discretization: (a) mesh of the fluid domain, (b) mesh of external windshield.

This study carries out a mechanical co-simulation using STAR-CCM+ and Abaqus. The mechanical co-simulation differs from the file-based method; in the co-simulation, data are automatically exchanged between Abaqus and STAR-CCM+ using the SIMULIA Co-Simulation Engine. Co-simulation involves a strong coupling between the two codes. Data are exchanged at frequent intervals that are called coupling steps. This level of communication between the solvers allows for obtaining a full solution across the fluid–solid interface. STAR-CCM+ and Abaqus run simultaneously. In mechanical coupling, the fluid domain passes traction loads to the solid domain (pressure and wall shear stress), and the solid domain passes displacements to the fluid domain. In the solid domain, the traction loads are applied to the surface of the solid structure. In the fluid domain, the displacements are used as an input to the mesh morpher [34]. For the FSI simulation, the relevant parameters are shown in Table 1. The simulation time step is determined according to the minimum volume grid distribution around the train body and the incoming flow velocity, which ensures that the CFL of the numerical calculation in this study is less than 1. Owing to the large deformation of the U-shaped rubber external windshield structure under the aerodynamic load, the relative movement between molecules in the structure is small, that is, the rubber molecular chain of the external windshield only bears a relatively small deformation, and the corresponding stress can be well approximated from the traditional elastic analysis. Based on this, we assume that the rubber material used in the external windshield is linear elastic and isotropic [35]. The comparison between the full-scale test results and the numerical simulation results shows that the small deformation assumption for the rubber external windshield has certain applicability in the problems studied in this paper. This study assumes that the rubber external windshield structure has linear elastic characteristics under the aerodynamic load, and takes into account the influence of structural damping. Additionally, the Rayleigh damping factor is considered to be $\alpha = 0.125$ and $\beta = 0.00159$.

Table 1. The relevant parameters for the FSI simulation.

Type	Fluid Model	Solid Model
Mesh Elements	Hexahedral mesh	C3D8R elements
Material Properties	μ : 1.85508×10^{-5} Pa.S ρ : 1.18415 kg/m^3	E: 7.97 Mpa σ : 0.4995 ρ : 1300 kg/m^3
Models	URANS(SST k-omega)	Elastic material
Maximum Time-Step	2×10^{-5} s	2×10^{-5} s
Total Simulation Time	4 s	4 s

3. Numerical Validation

Tang et al. [14] carried out a full-scale test of an HST exterior windshield at the running speed of 350 km/h; the dynamic characteristics of the exterior windshield were tested and the test contents and results described in detail. In this paper, a numerical simulation model

of FSI is established based on the full-scale test. To verify the reliability of the FSI numerical method in this paper, and the FSI simulation results of the rubber external windshield of Case 1 are compared with the full-scale test. Additionally, the simulation settings for the FSI of the other schemes are highly consistent with that of Case 1, and only the exterior windshield structural sections are changed to ensure the reliability of the comparative analysis for the results of different windshield schemes.

Figure 5 shows the surface pressure of the rubber external windshield at 350 km/h running speed, intercepted from the time-history curve for the full-scale test and compared with the surface pressure at the stable stage of the FSI calculation results. Figure 6 shows the main vibration frequencies for the dynamic response of the rubber external windshield structure under the aerodynamic force in the numerical simulation and the full-scale test. Through comparison, the main vibration frequencies of the rubber external windshield are similar. Table 2 compares the average pressure value for the full-scale test and numerical simulation together with the dominant frequency of the pressure fluctuation and the dominant frequency of vibration for the rubber external windshield. Compared with the full-scale test, the pressure and displacement results for the rubber external windshield structure obtained by the two-way coupling simulation method have definite consistency.

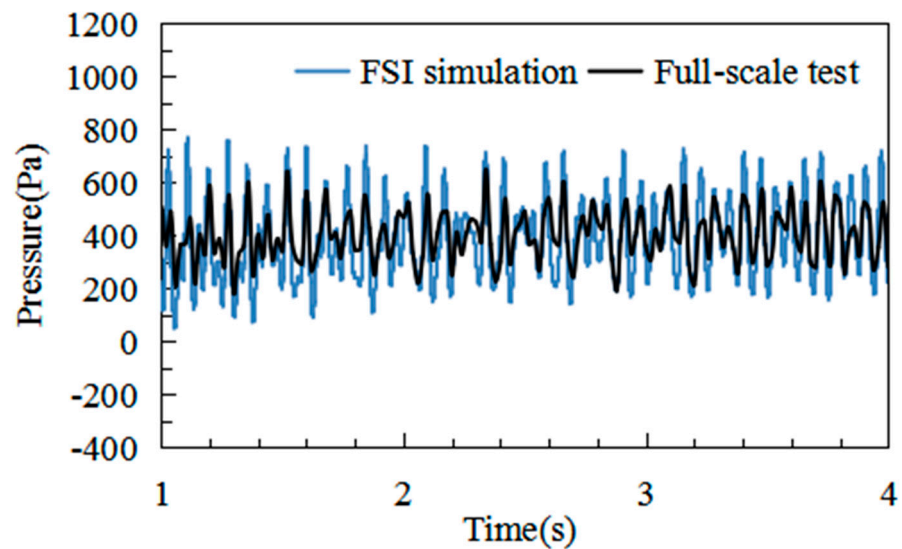


Figure 5. Data for the surface pressure on the rubber external windshield.

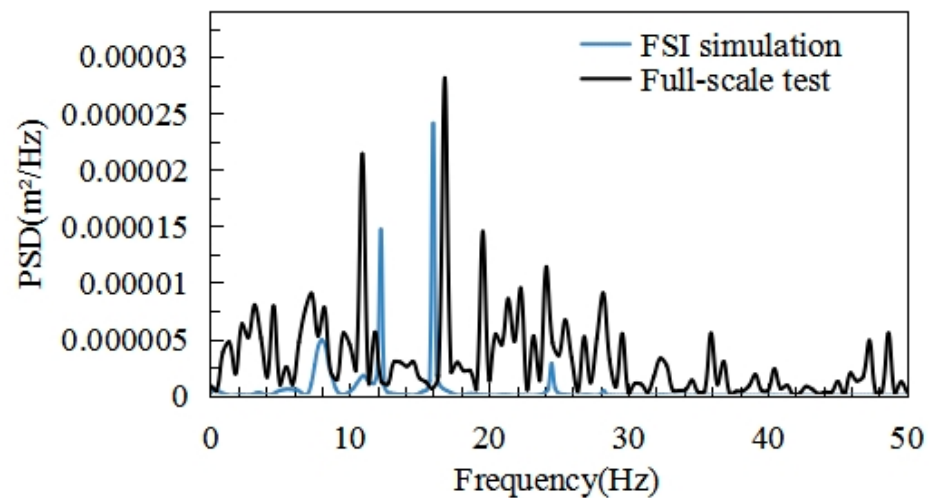


Figure 6. PSD of the vibration signal of the windshield.

Table 2. Comparison of pressure and vibration data for the FSI simulation and the full-scale test.

Type	FSI Simulation	Full-Scale Test	Relative Deviation
AVG of Pressure/Pa	387.42	404.08	4.3%
PSD of Pressure/Hz	16.0	16.3	1.9%
PSD of Vibration/Hz	16.0	16.8	5.0%

4. Results and Discussion

When the train is running at a high speed, the airflow around the train body is complex and in a turbulent state. In addition, strong flow separation occurs when the air flows through the connection between the carriages, which makes the aerodynamic load borne by the windshield structure very complicated; the vibration response and structural deformation of the rubber external windshield is easily caused under the strong aerodynamic action. It seriously affects the aerodynamic stability and structural safety of rubber external windshield. In this paper, the dynamic response characteristics of the rubber external windshield structure of three different schemes are compared. To avoid the influence of the streamline of the head train on the aerodynamic performance analysis of the external windshield, the second group of side external windshield structure between the middle carriage and the tail carriage was selected for FSI simulation and dynamic response analysis.

4.1. Pressure Distribution and Flow-Field Structure at the Outer Windshield

To obtain the initial flow-field characteristics of the external windshield without deformation and vibration response, the surface pressure distribution and flow-field structure around the external windshield between the middle carriage and the tail carriage are shown. Taking the rubber external windshield of Case 1 as an example, three horizontal sections of the external windshield with different spatial heights are selected. The heights of sections 1 to 3 from the ground are 1.5, 2, and 3 m, respectively, as shown in Figure 7. Owing to the good symmetry of the train body and the external windshield structure, the side structure of the external windshield was emphasized in the analysis of the initial flow field. The side part of the rubber outer windshield installed on the middle carriage was defined as W1, and the side part of the rubber external windshield installed on the tail carriage was defined as W2.

Figure 8 shows a cloud diagram of the time-average pressure distribution on one side of sections 1 to 3 in the initial flow field. Figure 9 shows the pressure distribution on the outer contour line of the windshield in sections 1 to 3. The inner side of the windshield is defined as the starting point, and the pressure distribution laws on the three sections at different heights are quantitatively displayed along the outer contour line of the windshield. According to the principle of relative wind speed, the W1 capsule dome is on the leeward side and the W2 capsule dome is on the windward side, determined by comparing the cloud diagram of the time-average pressure of the different height horizontal sections shown in Figure 8. Since there is an installation distance of 20 mm between the vehicle body and the outer windshield, when the air flows through the connection between the vehicle body and W1, a negative pressure area is generated, and when the air flows through the connection between W2 and the vehicle body, a positive pressure and negative pressure area are formed. The sidewall of the windward side W2 is affected by positive pressure, while the sidewall of the leeward side W1 is mainly affected by negative pressure. With the change in the section height, the pressure distribution around the outer windshield is quite different. In S2, the positive pressure on the outer wall of W2 and the negative pressure on the outer wall of W1 are greater than S1 and S3, and there is a small negative pressure area at the arc position outside W1 and at the top of the arc of W2. Figure 9 shows the quantitative results of the pressure distribution on the outer surface of the windshield at three different height sections. It can be seen from the comparison that the pressure distribution on the inner wall surface of the outer windshield of sections 1 to 3 is similar

and positive. The change in height mainly affects the top of the capsule arc of the rubber external windshield, and the pressure environment of S2 is worse than that for S1 and S3. Since section S2 is located at the widest position of the vehicle body, the airflow is less affected by the ground and the vehicle roof, and the airflow rate here is fast, resulting in a higher negative pressure distribution on the outer side of W1 and a higher positive pressure distribution on the outer side of W2 than on the other two sections.

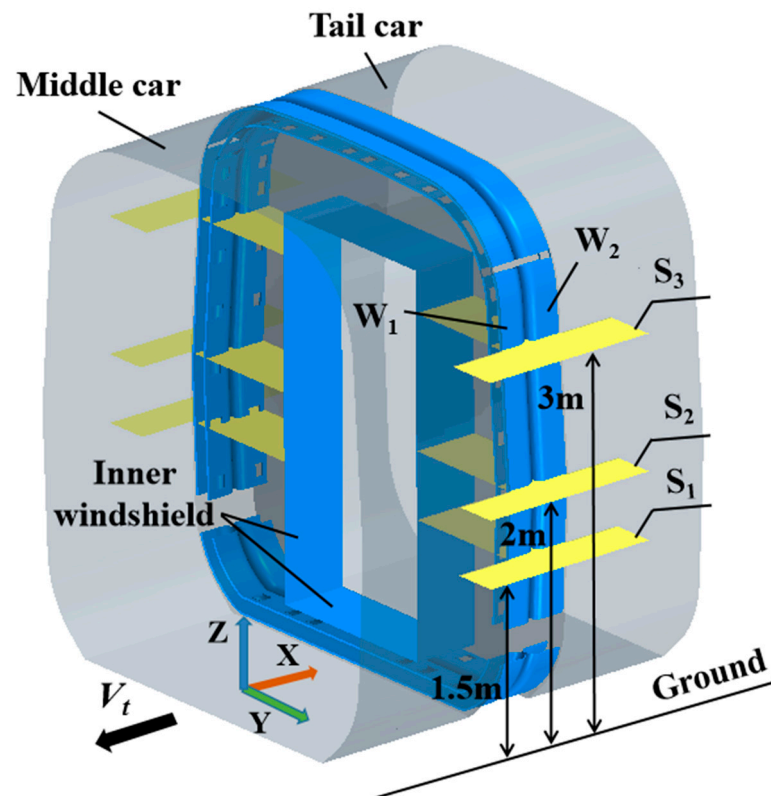


Figure 7. The position distribution of the horizontal section.

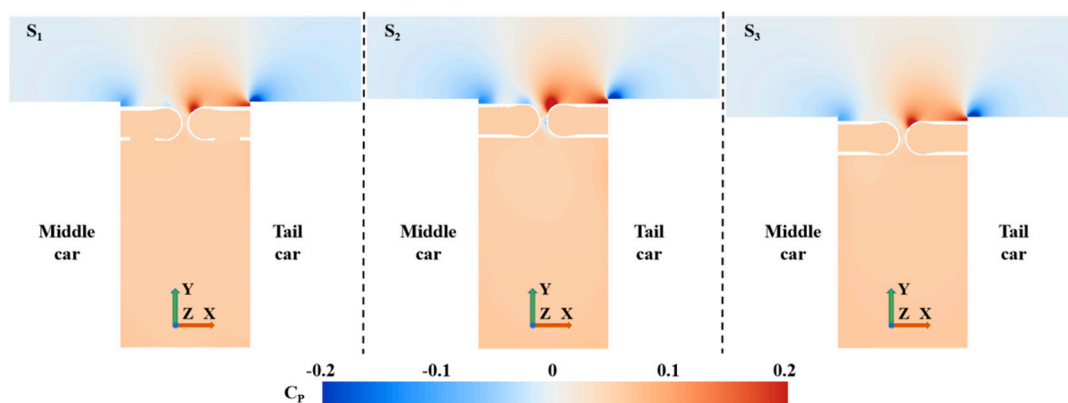


Figure 8. Average pressure distribution at the cross-section under the initial flow field.

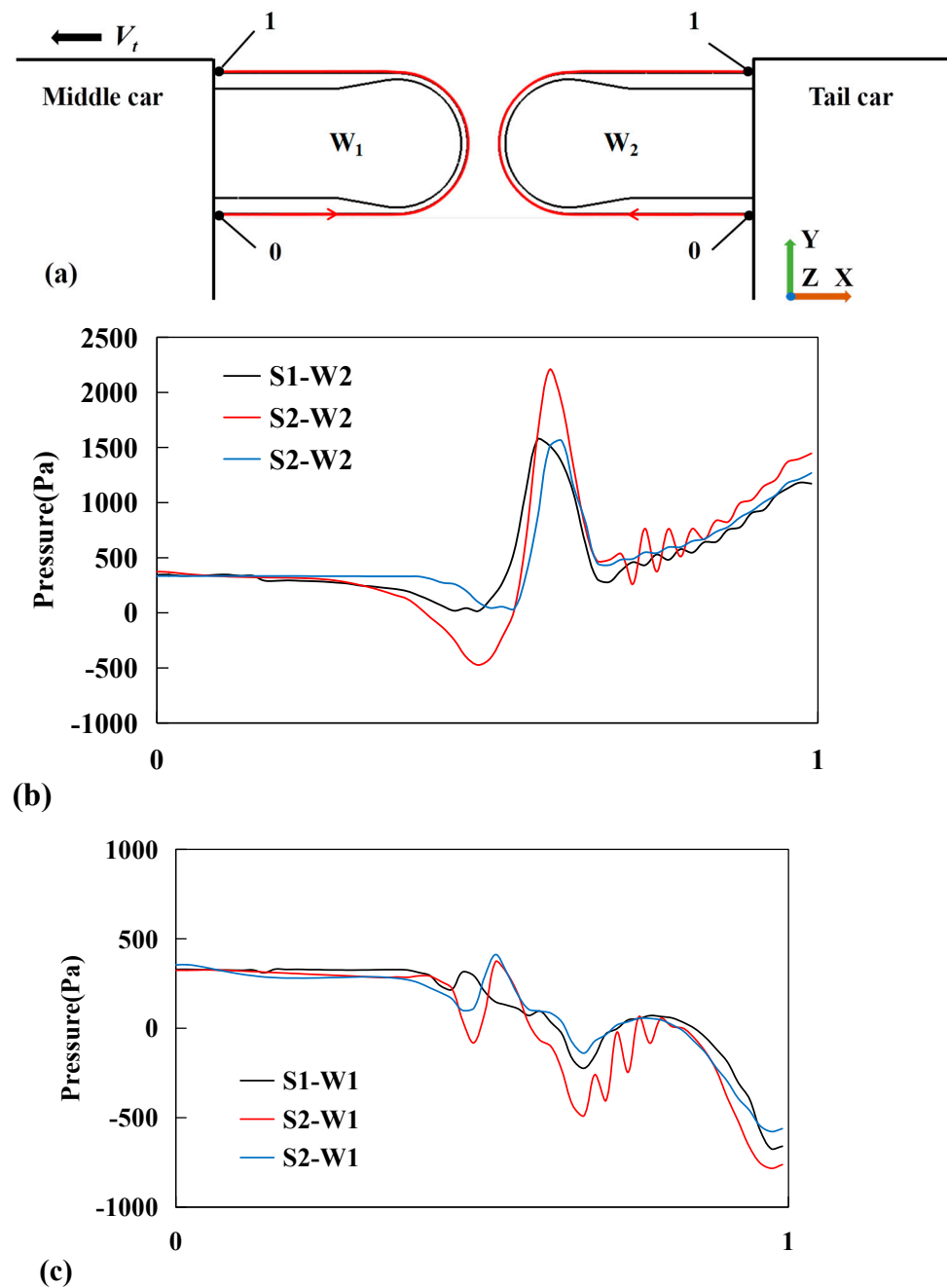


Figure 9. Pressure distribution of the windshield outer surface contour with different height sections: (a) schematic diagram of the windshield outer surface contour, (b) W2 windshield, (c) W1 windshield.

Figure 10 shows the time-averaged flow-field structure of sections 1 to 3 in the initial flow-field state. Through comparison, it can be concluded that the air flows into the cavity between the exterior windshield and the interior windshield through the camber and gap of the exterior windshield and produces a relatively high-speed rotary movement in the cavity. With the change in train height, the flow-field structure of the three sections has different changes. It can be seen from S1 and S2 that the air flows into the cavity from the gap and rotates clockwise with respect to the center of the cavity. Relative to the time-averaged velocity field of S1, the main vortex at S2 moves outward to the windshield and forms multiple vortices in the cavity. The airflow direction at S3 is opposite to that at S1 and S2, and the airflow at S3 rotates counterclockwise with respect to the center of the cavity. From this point of view, between S2 and S3, the outer windshield structure is subject to the

shear action generated by the fluid, which is very unfavorable for the safety of the outer windshield structure.

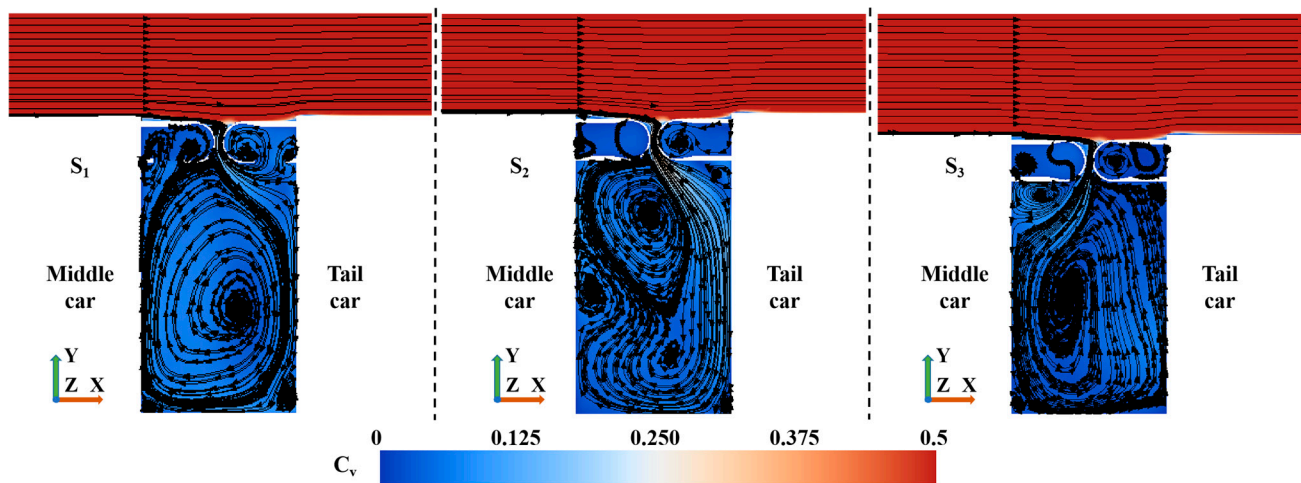


Figure 10. Average flow-field structure of the cross-section under the initial flow-field state.

From the view of the flow-field structure, the direction of aerodynamic load on the windward side and leeward side of the outer windshield is different. W1 is pulled toward the exterior of the vehicle body by air, and W2 is pressed toward the inside of the vehicle body by air. Therefore, the two opposite outer windshield capsules have a movement trend of dislocation. Therefore, the distribution of aerodynamic pressure around the carriage connection affects the stress state of the rubber external windshield, and leads to the deformation and movement trend of the rubber external windshield. In turn, the dynamic response of the rubber external windshield causes changes in the surrounding airflow, resulting in the redistribution of aerodynamic pressure on the surface of the rubber windshield, thus forming the FSI problem of the interaction between the aerodynamic force and the rubber external windshield structure.

4.2. Time- and Frequency-Domain Analysis of Vibration Displacement

To analyze the dynamic characteristics of the rubber external windshield under the FSI of aerodynamic load and structure, the dynamic response of the rubber external windshield are analyzed in time domain and frequency domain. According to the analysis in Section 4.1, the aerodynamic load environment at S2 is worse. Therefore, it is selected to establish displacement measuring points on S2, as shown in Figure 11. Measuring points d1 and d2, respectively, are located at the intersection of the sidewall and the arc of leeward W1 and windward W2. Measuring points d3 and d4, respectively, are located at the center of arc top of leeward W1 and windward W2, thus ensuring that the layout of displacement measuring points in the outer windshield structure for the three schemes is consistent.

4.2.1. Time-Domain Analysis

Figure 12 shows the displacement curve for the measuring points at different positions along the y-axis with time when the aerodynamic response of the three rubber external windshield schemes occurs under the aerodynamic load. To better analyze the time-domain characteristics of the aerodynamic response for the rubber external windshield, the amplitude change in the displacement time-history curve was divided into two stages (0~1 s and 1~4 s). The mean displacement of different vibration stages and the root mean square (RMS) value of time-domain displacement are analyzed, as shown in Table 2. The RMS of the time-domain displacement signal is calculated without using a window function and filter; the formula is as follows:

$$RMS = \sqrt{\frac{1}{k+1} \sum_{i=0}^k y_i^2} \tag{11}$$

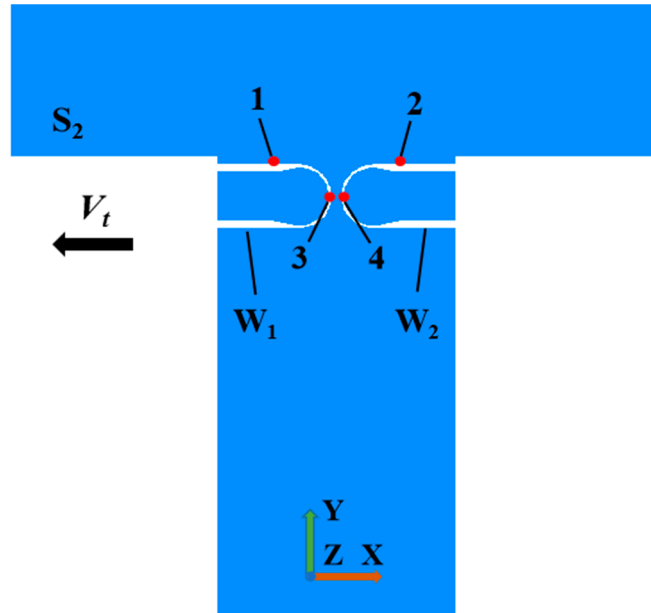


Figure 11. Monitoring points.

Calculate the sum of squares of all amplitudes of the time series, divide by the total number of sample points, and finally take the square root, where $k + 1$ represents the total number of sample points in the calculated interval.

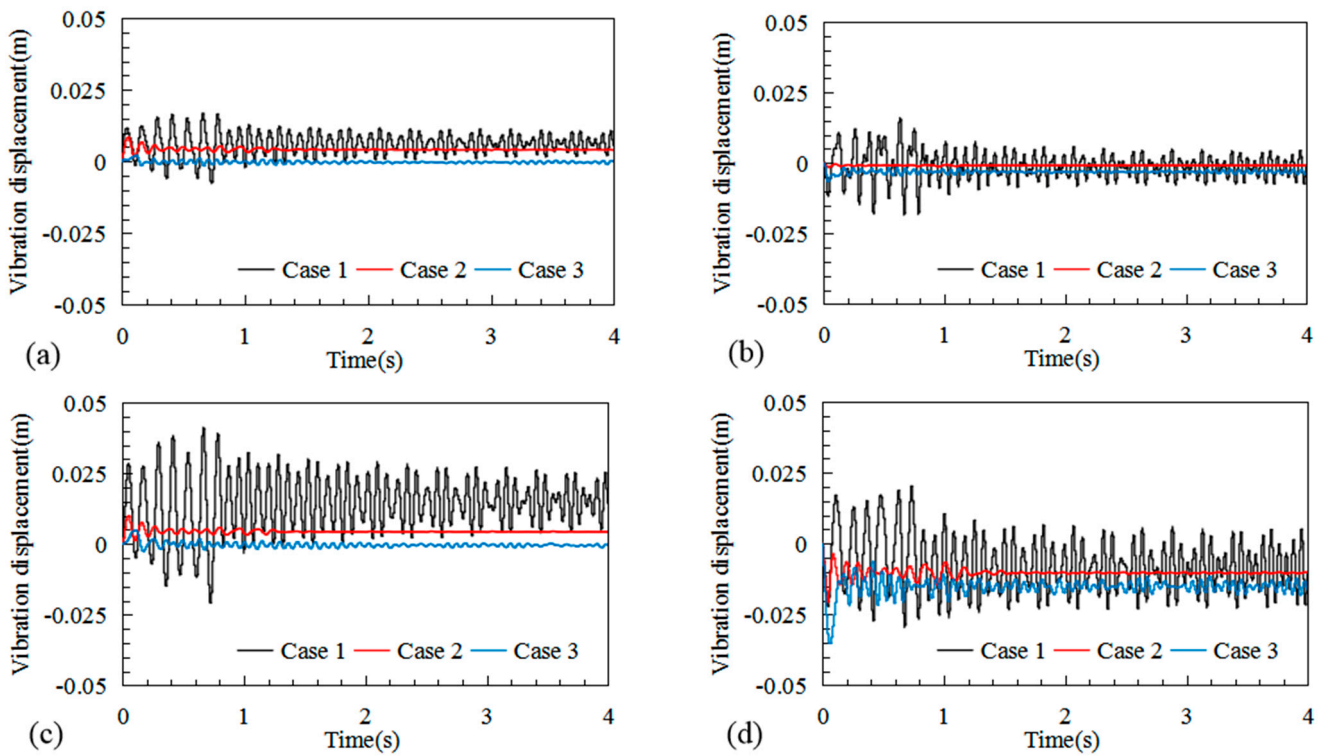


Figure 12. Displacement time-history curve: (a) d1, (b) d2, (c) d3, (d) d4.

By comparing the displacement time-history curves for the rubber external windshield structure, the vibration displacement state of the three schemes can be observed. It can be seen from Figure 12 that the vibration displacement and amplitude of the external windshield structure in Case 1 along the direction perpendicular to the vehicle body surface are significantly greater than those in Case 2 and Case 3. As the thickness of the straight walls on both sides of the outer windshield capsule is greater than the arc top, and the straight walls on both sides of the capsule are connected with the mounting bracket, the fluctuating amplitude of points d1 and d2 is smaller than that of points d3 and d4 in the middle of the arc of the U-shaped capsule. At the initial stage of the dynamic response of the outer windshield, there is not yet a dynamic balance stage between aerodynamic force, inertial force, and elastic force, which causes the vibration amplitude to change significantly with time, such as within 0~1 s of the vibration stage. When the interaction among aerodynamic force, inertial force, and elastic force reaches a dynamic balance, the amplitude and period of vibration remains relatively stable.

Table 3 shows the average and RMS values for the displacement measuring points in the two dynamic response stages, and quantitatively compares the displacement and vibration intensity between the three external windshield schemes. According to the data in the table, the maximum displacement of external windshield d3 in Case 1 is 15.1 mm, the maximum displacement of outer windshield d4 in Case 3 is 15.8 mm, and the maximum displacement of outer windshield in Case 2 is 10.4 mm, less than that in Case 1 and Case 3. The vibration displacement direction of the rubber external windshield can be judged by the positive and negative displacement measuring points. For example, in the two stages of vibration response of the external windshield in Case 1 and Case 2, the measuring points d1 and d3 are both negative values, and the measuring points d2 and d4 are both positive values, Therefore, W1 is displaced from the initial state to the exterior of the vehicle body, and W2 is displaced from the initial state to the inside of the vehicle body, that is, phase displacement movement is generated. In Case 3, the deformation laws of W1 and W2 are the same as those of Case 1 and Case 2 in the initial stage of vibration. In the stage of vibration stability, however, W1 and W2 in Case 3 both move toward the inner side of the vehicle body. For RMS amplitude, the dynamic response starting stage of the rubber external windshield is greater than the dynamic response stability stage. In the dynamic response starting stage, the maximum RMS amplitude of d3 on W1 on the leeward side is 15.6 mm. In the vibration stability stage, the vibration intensity of Case 1 is the largest, followed by Case 3, and Case 2 is the smallest. By comparing the vibration displacement results for the rubber external windshield along the Y-axis direction of the three schemes, it can be seen that the outer windshield of Case 1 produces more severe deformation vibration under the action of aerodynamic load, and the stability of Case 2 is relatively better than that for Case 1 and Case 3.

Table 3. Mean value of displacement measuring points and RMS amplitude (mm).

Case	Segments	Type	d1	d2	d3	d4
Case 1	0~1 s	AVG	5.7	-0.2	11.6	-3.9
		RMS	6.1	7.5	15.6	13.1
	1~4 s	AVG	6.3	-1.3	15.1	-8.7
		RMS	3.0	3.5	7.5	8.0
Case 2	0~1 s	AVG	4.4	-0.9	4.6	-10.4
		RMS	1.2	0.2	1.5	2.9
	1~4 s	AVG	4.1	-0.9	4.3	-10.3
		RMS	0.3	0.1	0.4	1.0
Case 3	0~1 s	AVG	0.0	-3.2	0.2	-15.8
		RMS	0.7	1.0	1.5	5.6
	1~4 s	AVG	-0.3	-3.2	-0.5	-15.1
		RMS	0.3	0.4	0.5	1.5

4.2.2. Frequency-Domain Analysis

To compare the dynamic response characteristics of the rubber external windshield in the three schemes, the frequency spectrum of the two time stages of the displacement curve is analyzed. Figure 13 shows the power spectral densities (PSD) for d1, d2, d3, and d4 at the initial stage of windshield vibration for the three schemes. Figure 14 shows the power spectral densities for d1, d2, d3, and d4 in the vibration response stability stage of the rubber external windshield for the three schemes.

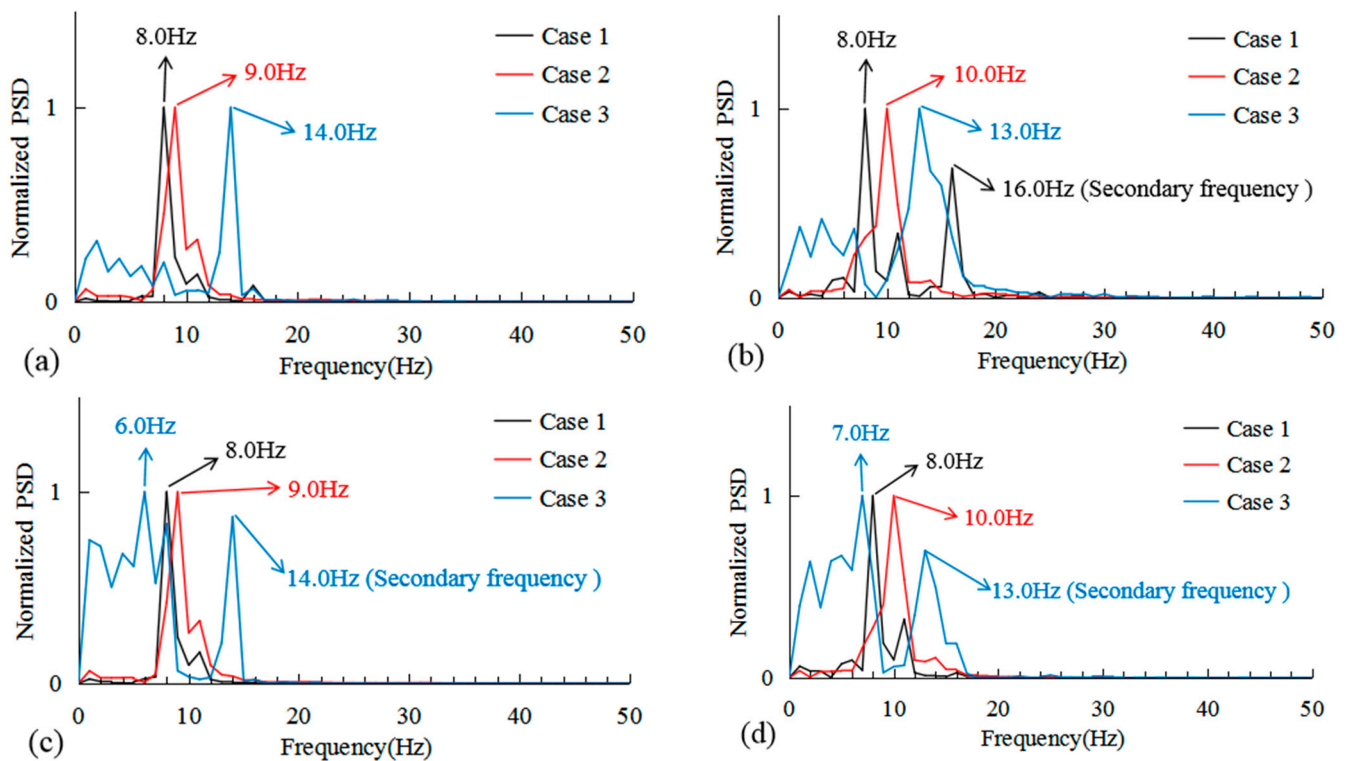


Figure 13. PSD in the vibration response initial stage: (a) d1, (b) d1, (c) d3, (d) d4.

The displacement response frequency for the three external windshield schemes in two different dynamic response stages is shown in Figure 14. In Case 1, the vibration frequency of d1, d2, d3, and d4 is the same at the initial dynamic response stage, and the main frequency is 8 Hz. In the vibration stability stage, the dominant frequency of vibration for each measuring point is 16 Hz. In Case 2, at the initial vibration stage, the dominant frequency of the rubber external windshield vibration is 9 Hz for W1 and 10 Hz for W2, and the dominant frequency of the vibration at each measuring point is 7 Hz in the vibration stability stage. In Case 3, at the initial vibration stage of the rubber external windshield structure, the dominant frequency of vibration at measuring points d1, d2, d3, and d4 is 14, 13, 6, and 7 Hz, respectively. In the vibration stability stage, the dominant frequency of vibration at measuring points d1, d2, and d4 is 15.7 Hz, and that of d3 is 14 Hz. By comparing the vibration frequencies for the two vibration stages of the rubber external windshield for the three schemes, it is found that from the initial vibration stage to the vibration stability stage, the vibration frequency of the rubber external windshield for Case 1 and Case 3 increases, while the vibration frequency for Case 2 decreases. With the change in the geometric shape of the windshield structure, the natural frequency and structural stiffness of the rubber external windshield are different, which leads to the change in the vibration frequency for the windshield under the aerodynamic action. Compared with Case 1 and Case 3, the structural stability of the windshield in Case 2 is better.

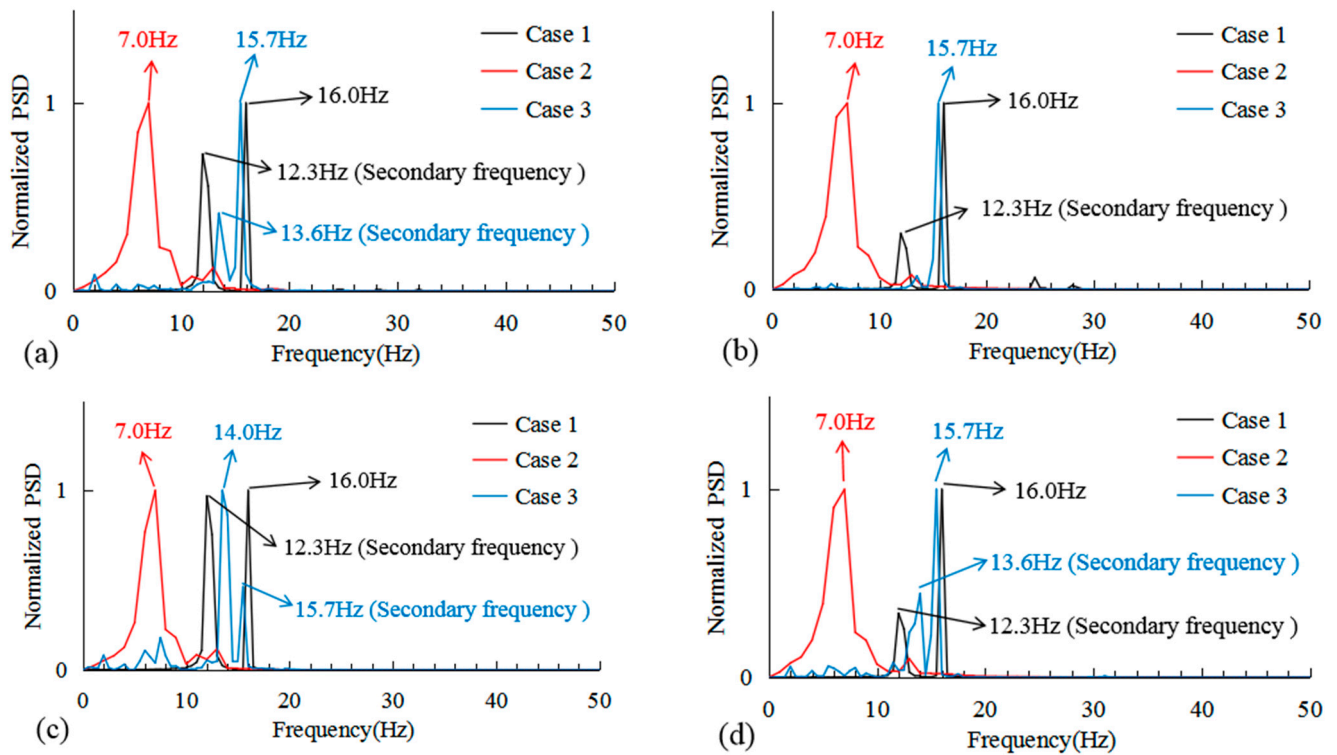


Figure 14. PSD in the vibration response stability stages: (a) d1, (b) d1, (c) d3, (d) d4.

4.3. FSI Behavior Characteristics of the Rubber External Windshield

To analyze the FSI characteristic between the windshield structural dynamic response and the air flow around the carriage connection, the FSI calculation for the rubber external windshield in Case 1 is taken as an example to show the relationship between the deformation movement and the force acting on the external windshield. Figure 15 shows several characteristics of the surrounding flow-field movement and structural deformation movement during the reciprocating vibration period for the rubber external windshield. Figure 15a shows the initial flow-field state before the external windshield is deformed. It can be seen that the air enters the cavity between the external windshield and the internal windshield along the top arc of W2 and flows clockwise along the vehicle body end wall. The air exerts pressure on the W2 windshield toward the cavity and thrust on W1 toward the outside of the vehicle body. Under the action of aerodynamic force, W1 and W2 form deformation and dislocation. W1 deforms to the outside of the vehicle body and reaches the maximum displacement of eversion. W2 deforms to the inside of the vehicle body. At this time, air in the cavity flows out along the arc at the top of W1, as shown in Figure 15b. When W1 turns outward to the maximum displacement, the elastic force is the largest, and the air in the cavity flows out, causing the pressure in the cavity to drop, so W1 rebounds, as shown in Figure 15c. When W1 rebounds to the initial state, owing to the inertial force, it continues to deform a certain distance to the inner side of the vehicle. At this time, the air continues to enter the cavity along the arc at the top of W2, as shown in Figure 15d. In this way, the aerodynamic force interacts with the outer windshield structure to form a typical periodic vibration process.

Figure 16 shows the time-history relationship between the resultant force on the rubber external windshield and the displacement of the windshield during the initial and stable vibration stages. It can be seen that the deformation movement of the rubber external windshield is greatly affected by the inertial force during the initial vibration stage, and the deformation amplitude is large and unstable. In the vibration stability stage of the rubber external windshield, the aerodynamic force, elastic force, and inertial force tend to be more

stable, and the rubber external windshield structure shows obvious periodic movement under the combined force.

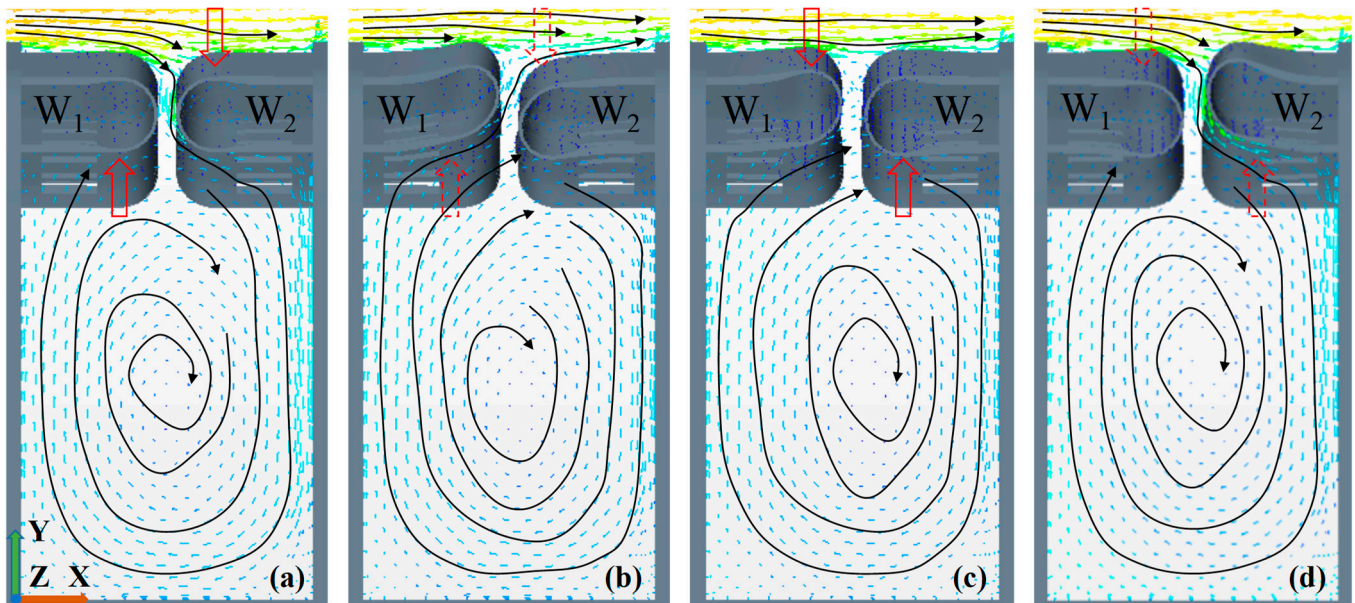


Figure 15. Characteristic morphology of flow-field movement and structure deformation during the vibration period: (a) initial state before vibration, (b) maximum displacement state of W1 eversion, (c) intermediate state of W1 rebound, (d) maximum displacement state of W2 eversion.

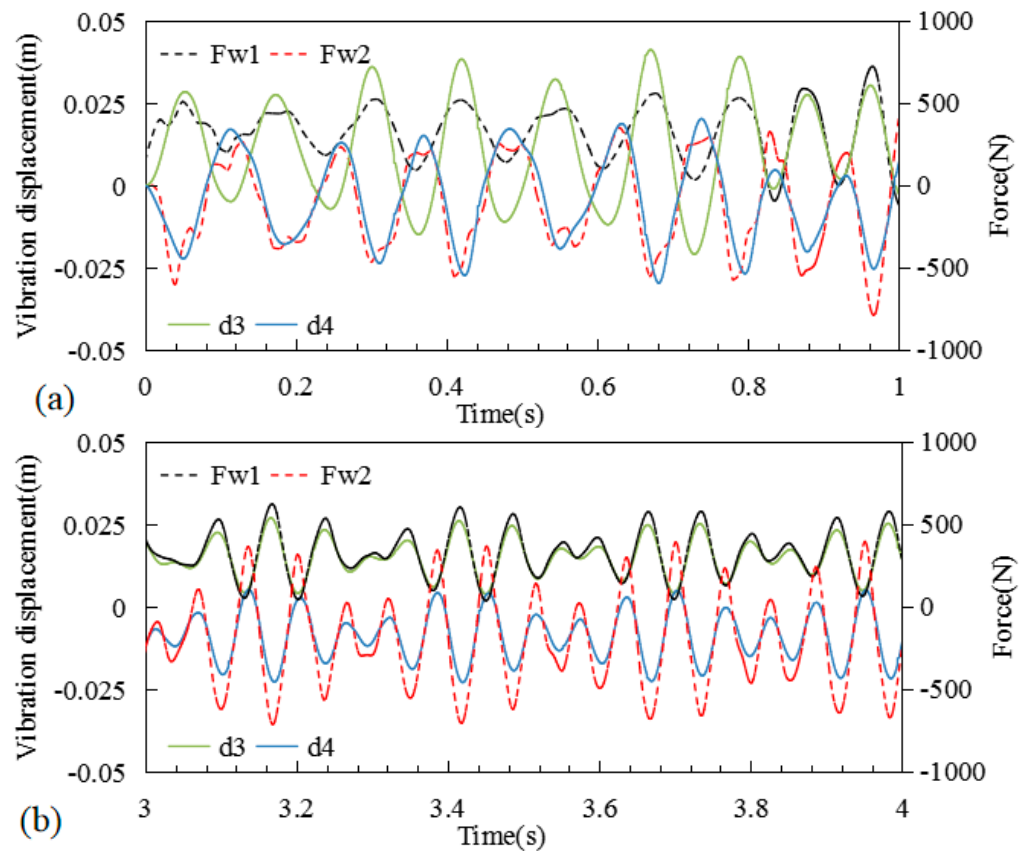


Figure 16. The relationship between displacement and resultant force in the initial and stable stages of vibration: (a) initial stage of vibration, (b) stable stage of vibration.

4.4. Comparison of Periodic Deformation Forms in the Outer Windshield

4.4.1. Comparison of Periodic Deformation Forms in the Outer Windshield

Figures 17 and 18, respectively, show the initial and stable vibration stages of the outer windshield for the three schemes, the relative displacements of d3 and d4 at different time nodes, and the deformation patterns of several time nodes for the outer windshield at S2 in the vibration periodic.

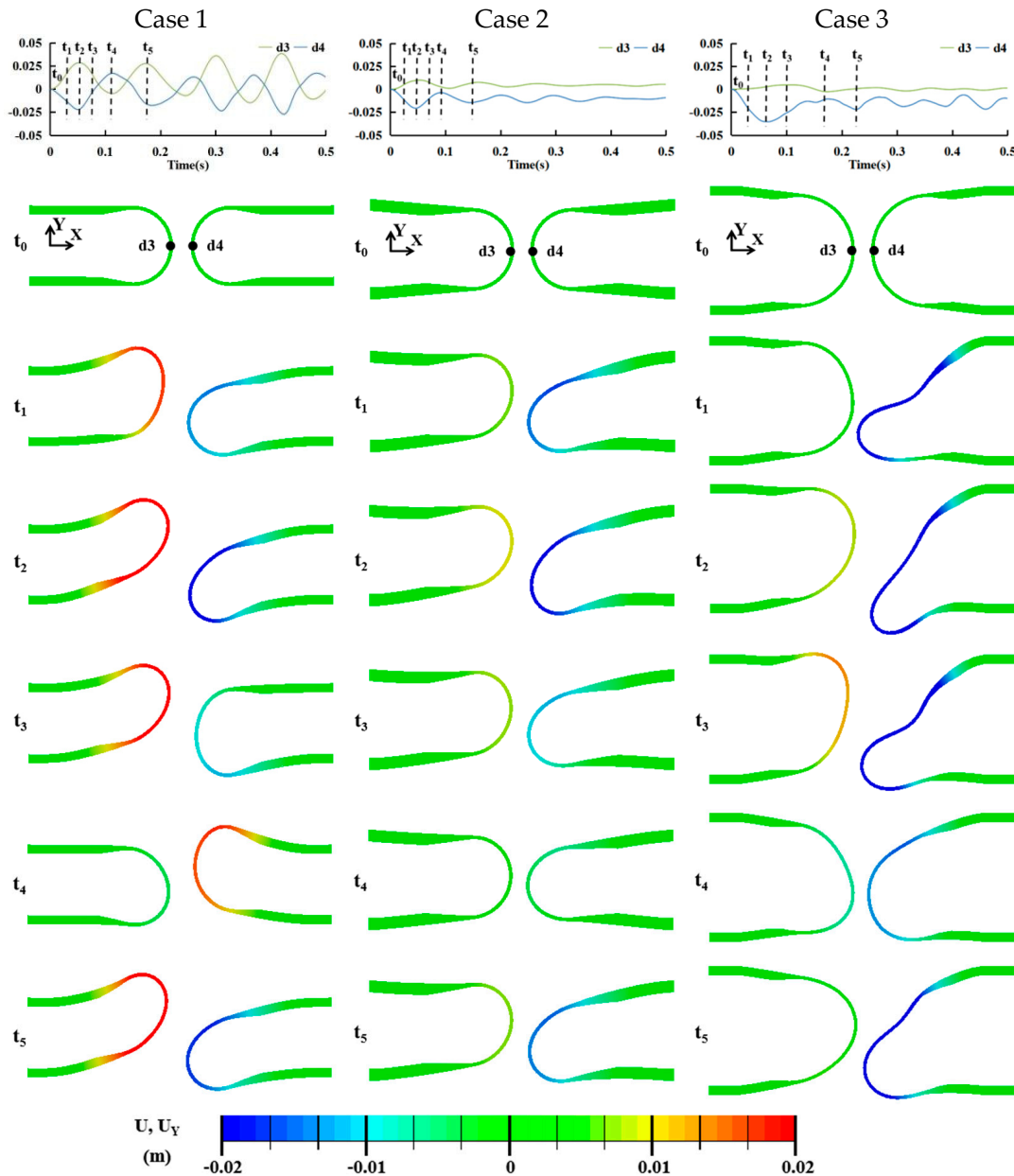


Figure 17. Comparison of typical deformation forms for the three schemes in the initial vibration stage.

By comparing the figures of the deformation patterns for the three external windshield schemes at the initial dynamic response stage, the movement trend and relative position of the rubber external windshield schemes during the vibration response process can be seen. Under the initial aerodynamic force, the rubber external windshield deforms and the deformation state of the rubber external windshield affects the distribution of the flow field. Under the interaction of aerodynamic force, elastic force, and inertial force, the external windshield produces continuous movement of deformation and rebound. The difference in the geometric structure of the outer windshield leads to an obvious difference in the force

and deformation resistance of the rubber external windshield. As the windshield structure of Case 1 is relatively light, the initial displacement of the rubber external windshield is large, and the periodic bending deformation in the overall structure is greater than that for Case 2 and Case 3. In Case 3, the width of the rubber external windshield structure is large, and the dome structure is thinner than the whole structure, so the local deformation at W2 on the windward side is large. The width of the rubber external windshield structure in Case 2 increases, and the wall thickness on both sides increases, so the structural strength is larger, and the displacement generated is smaller than that in Case 1 and Case 3. At the stage when the dynamic response of the rubber external windshield tends to be stable, the interaction of aerodynamic force, inertial force, and elastic force is relatively stable, and the displacement amplitude of the windshield decreases. Case 1 shows a periodic movement with stable amplitude, and Case 2 and Case 3 almost maintain stable deformation under the action of aerodynamic force.

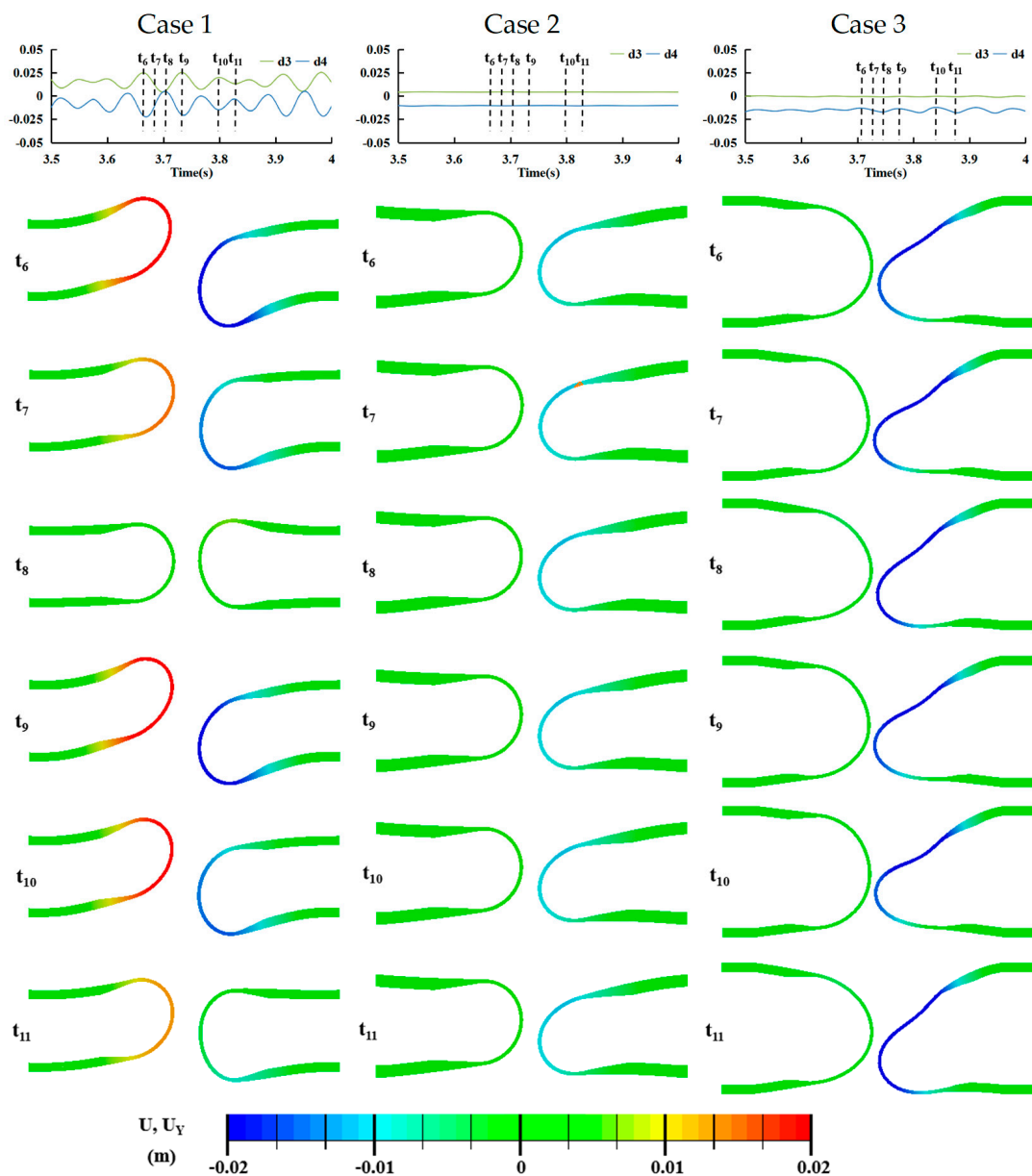


Figure 18. Comparison of typical deformation forms for the three schemes in the stable vibration stage.

4.4.2. Stress Distribution in the Rubber External Windshield

Through analysis of the dynamic response characteristics for the rubber external windshield, it is found that the deformation form of the rubber external windshield structure in different schemes under the action of aerodynamic force is quite different. The large deformation results in a large stress distribution in the rubber external windshield structure. Mises stress is an equivalent stress based on the shear strain energy; the calculation formula is as follows

$$\sigma = \sqrt{\frac{(\sigma_1 - \sigma_2)^2 + (\sigma_2 - \sigma_3)^2 + (\sigma_3 - \sigma_1)^2}{2}} \tag{12}$$

where $\sigma_1, \sigma_2,$ and σ_3 refer to the first, second, and third principal stresses, respectively. It is the fourth intensity theory and the distortion energy density theory. This theoretical task distortion energy density is the main factor causing material yield. The material yields when the Mises stress reaches the yield stress value.

For the three schemes, Figure 19 shows a comparison of the maximum stress distribution in the dynamic response process for the rubber external windshield side. It can be observed that the stress in Case 1 is mainly concentrated at the lower process hole and the fixed support during the vibration response of the rubber external windshield, and the stress value is significantly higher than that in the other two schemes. Since the vibration patterns of Case 1 and Case 2 are the same, the stress concentration positions of the two schemes are close. Because the top of the arc in the rubber external windshield structure for Case 3 is weak, the deformation at the top of the arc under the action of aerodynamic force is the largest. The stress concentration location is mainly distributed on the top of the rubber outer windshield on the windward side, and the stress near the roof is greater than other locations.

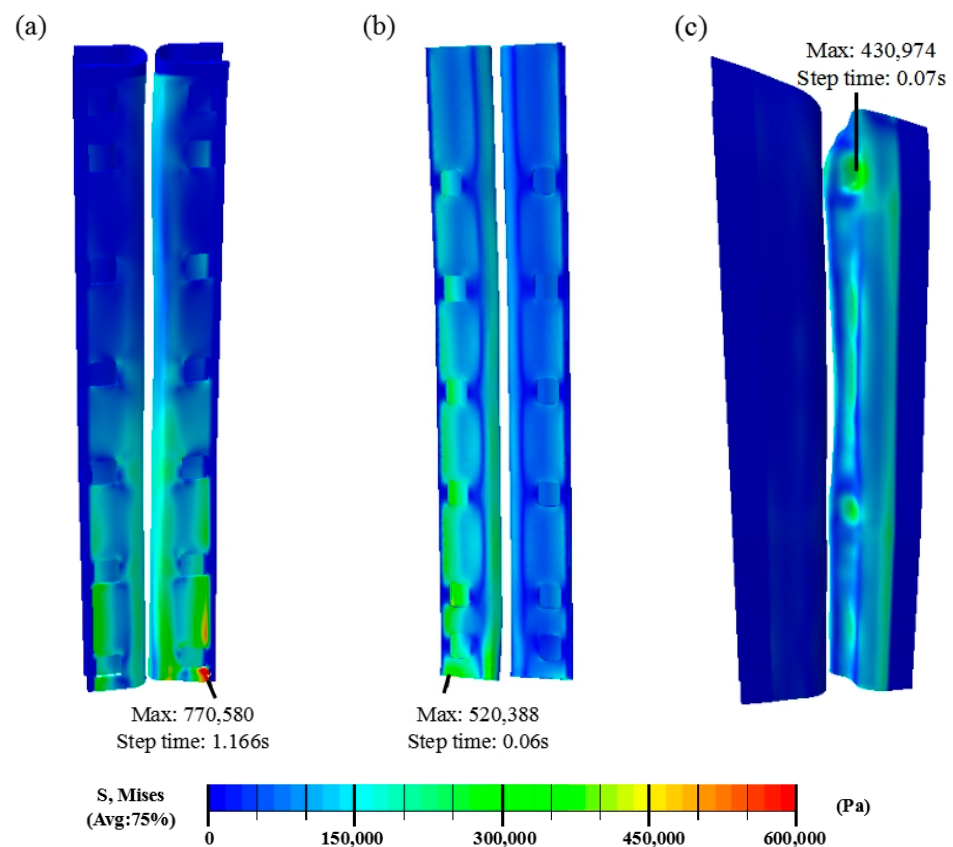


Figure 19. Stress concentration location: (a) Case 1, (b) Case 2, (c) Case 3.

In the actual application process, the fracture location of the rubber external windshield structure in Case 1 is shown in Figure 20. The fracture location of the rubber external windshield structure in Case 1 is the same as the stress concentration location in the FSI simulation, indicating that the FSI method has certain reference value for structural reliability analysis.

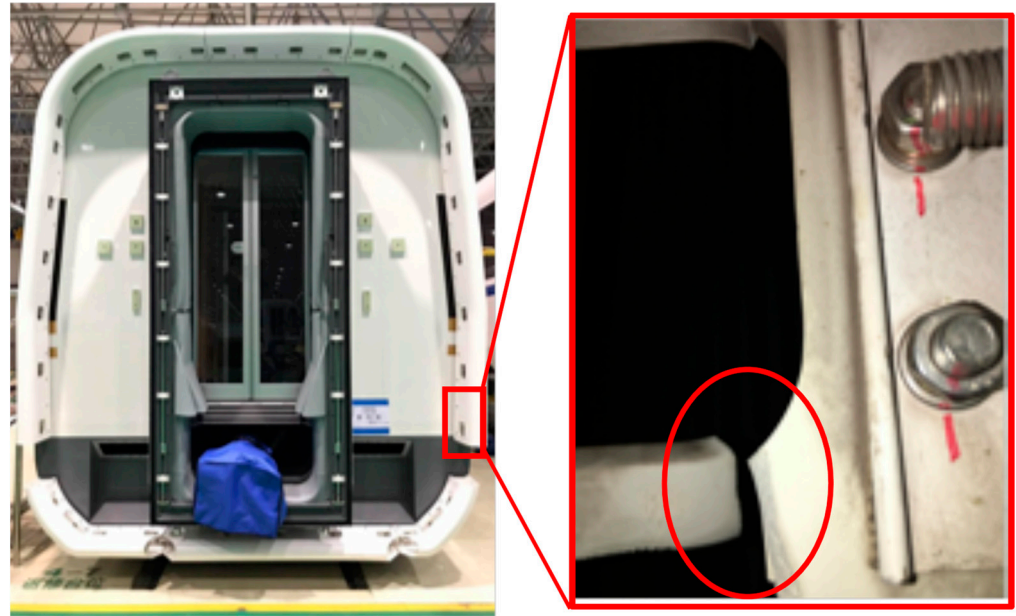


Figure 20. Fracture position in the rubber external windshield structure for Case 1.

5. Conclusions and Future Work

The different geometric structures of the outer windshield section lead to a large difference in its stiffness and natural frequency, making the aerodynamic stability of the outer windshield for different structural schemes vary under the same application environment. In the present study, the FSI method is adopted to investigate the aerodynamic stability of three different schemes of rubber external windshield structure; the following conclusions are drawn:

- (1) The airflow around the rubber external windshield at the end of the HST carriage is complex, and the air flows into the cavity along the outer windshield surface, resulting in an uneven pressure distribution on the outer surface of the rubber external windshield. The cavity interior generally maintains a positive pressure state. The outer side of the windshield on the leeward side is affected by negative pressure, and the outer wall of the windshield on the windward side is affected by positive pressure, resulting in an obvious force trend of relative dislocation, which is very unfavorable to the aerodynamic stability of the outer windshield.
- (2) By comparing the deformation form and vibration response frequency of the three rubber external windshield schemes, it can be concluded that the deformation of the rubber external windshield in Case 2 is significantly lower than the other two schemes, and the dynamic stability is also better. Increasing the thickness of the sidewall of the rubber external windshield can improve the stiffness of the outer windshield. However, when the distance between the sidewalls of the rubber external windshield increases, the insufficient thickness increase at the top of the arc causes greater deformation at the top of the arc.
- (3) By comparing the stress distribution of the structure response under the aerodynamic load of the outer windshield of the three schemes, it can be concluded that the stress in the outer windshield of Case 1 is mainly concentrated at the lower process hole and the fixed support during the vibration process. The stress value is significantly

greater than the other two schemes, leading to the greatest risk for fatigue damage in the outer windshield.

This research provides good support for evaluating the aerodynamic stability of rubber external HST windshields. The FSI method can accurately calculate the dynamic response characteristics for rubber external windshields in different structural schemes, which is of great significance for the optimal design of the outer windshield. In the next step, specific parametric research can be carried out on the shape and section size of the rubber external windshield, and the aerodynamic force can be reduced by optimizing the geometric shape of the windshield. By optimizing the structural section size parameters of the windshield, a better scheme to control the increase in the outer windshield mass while maximizing the stiffness and natural frequency of the rubber external windshield can be obtained.

Author Contributions: Conceptualization, M.-Z.T. and X.-B.L.; methodology, G.C. and M.Z.; formal analysis, J.Z. and B.S.; resources, X.-H.X.; writing—original draft, M.-Z.T.; writing—review and editing, X.-B.L.; supervision, X.-H.X.; funding acquisition, X.-H.X. All authors have read and agreed to the published version of the manuscript.

Funding: This work was supported by the National Key R&D program of China (grant no. 2020YFA-0710903); the Natural Science Foundation of Hunan Province (grant no. 2021JJ30849); the Graduate Student Independent Innovation Project of Hunan Province (grant no. CX20200196); and the Graduate Student Independent Innovation Project of Central South University (grant no. 2020zzts111 and 2020zzts117).

Institutional Review Board Statement: Not applicable.

Informed Consent Statement: Not applicable.

Data Availability Statement: Not applicable.

Acknowledgments: The authors acknowledge the computational resources provided by the High-Performance Computing Center of Central South University, China.

Conflicts of Interest: The authors declare no conflict of interest.

References

- Ding, S.S.; Li, Q.; Tian, A.Q.; Du, J.; Liu, J.L. Aerodynamic design on high-speed trains. *Acta Mech. Sin./Lixue Xuebao* **2016**, *32*, 215–232. [[CrossRef](#)]
- Ragunathan, R.S.; Kim, H.D.; Setoguchi, T. Aerodynamics of high-speed railway train. *Prog. Aerosp. Sci.* **2002**, *38*, 469–514. [[CrossRef](#)]
- Tian, H.Q. Review of research on high-speed railway aerodynamics in China. *Transp. Saf. Environ.* **2019**, *1*, 1–21. [[CrossRef](#)]
- Dai, W.Q.; Zheng, X.; Hao, Z.Y.; Qiu, Y.; Li, H.; Luo, L. Aerodynamic noise radiating from the inter-coach windshield region of a high-speed train. *J. Low Freq. Noise Vib. Act. Control* **2018**, *37*, 590–610. [[CrossRef](#)]
- Peters, J.L. Optimising aerodynamics to raise IC performance. *Railw. Gaz. Int.* **1982**, *138*, 817–819.
- Wu, J.M. Research on numerical simulation and noise reduction of aerodynamic noise in connection section of the high-speed train. *J. Vibroeng.* **2016**, *18*, 5553–5571. [[CrossRef](#)]
- Li, X.; Chen, G.; Krajnovic, S.; Zhou, D. Numerical Study of the Aerodynamic Performance of a Train with a Crosswind for Different Embankment Heights. *Flow Turbul Combust.* **2021**, *107*, 105–123. [[CrossRef](#)]
- Liang, X.; Zhang, X.; Chen, G.; Li, X. Effect of the ballast height on the slipstream and wake flow of high-speed train. *J. Wind Eng. Ind. Aerodyn.* **2020**, *207*, 104404. [[CrossRef](#)]
- Xia, C.; Wang, H.; Bao, D.; Yang, Z. Unsteady flow structures in the wake of a high-speed train. *Exp. Therm. Fluid Sci.* **2018**, *98*, 381–396. [[CrossRef](#)]
- Li, X.; Chen, G.; Zhou, D.; Chen, Z. Impact of different nose lengths on flow-field structure around a high-speed train. *Appl. Sci.* **2019**, *9*, 4573. [[CrossRef](#)]
- Niu, J.Q.; Zhou, D.; Liu, T.H.; Liang, X.F. Numerical simulation of aerodynamic performance of a couple multiple units high-speed train. *Veh. Syst. Dyn.* **2017**, *55*, 681–703. [[CrossRef](#)]
- Li, X.B.; Chen, G.; Wang, Z.; Xiong, X.H.; Liang, X.F.; Yin, J. Dynamic analysis of the flow fields around single- and double-unit trains. *J. Wind Eng. Ind. Aerodyn.* **2019**, *188*, 136–150. [[CrossRef](#)]
- Chen, G.; Li, X.; Zhang, L.; Liang, X.; Meng, S.; Zhou, D. Numerical analysis of the effect of train length on train aerodynamic performance. *AIP Adv.* **2022**, *12*, 025201. [[CrossRef](#)]

14. Tang, M.; Xiong, X.; Li, X.; Zhang, J.; Chen, G.; Wang, K. Vibration characteristics of outer windshield structures of high-speed trains based on fluid–structure interactions. *Nonlinear Dyn.* **2022**, *111*, 2111–2132. [[CrossRef](#)]
15. Horiuchi, M. Outline of Shinkansen High-Speed Test Train Type E955 (FASTECH360Z). *JR East Tech. Rev.* **2006**, *8*, 6–10.
16. Niu, J.; Wang, Y.; Zhou, D. Effect of the outer windshield schemes on aerodynamic characteristics around the car-connecting parts and train aerodynamic performance. *Mech. Syst. Signal Process.* **2019**, *130*, 1–16. [[CrossRef](#)]
17. Xia, Y.; Liu, T.; Gu, H.; Guo, Z.; Chen, Z.; Li, W.; Li, L. Aerodynamic effects of the gap spacing between adjacent vehicles on wind tunnel train models. *Eng. Appl. Comput. Fluid Mech.* **2020**, *14*, 835–852. [[CrossRef](#)]
18. Noh, H.M.; Koh, H.I.; Kim, S.W.; Chang, S.H. Aerodynamic noise reduction of a gangway in a high-speed train. In Proceedings of Meetings on Acoustics ICA2013. *Acoust. Soc. Am.* **2013**, *19*, 040087.
19. Cheng, F.; Xiong, X.H.; Tang, M.Z.; Li, X.B.; Wang, X.R. Impact of the gap distance between two adjacent external windshields of a high-speed train on surrounding flow characteristics: An IDDES study. *Eng. Appl. Comput. Fluid Mech.* **2022**, *16*, 724–745. [[CrossRef](#)]
20. Jiang, Q.; Zheng, G.; Zhao, G. Flutter Study on High Speed Train External Windshield by a Tight Coupling Method. In *Fluids Engineering Division Summer Meeting; American Society of Mechanical Engineers*: New York, NY, USA, 2019; Volume 59032, p. V002T02A050.
21. Nakhchi, M.E.; Rahmati, M. Direct numerical simulations of flutter instabilities over a vibrating turbine blade cascade. *J. Fluids Struct.* **2021**, *104*, 103324. [[CrossRef](#)]
22. van Loon, R.; Anderson, P.D.; van de Vosse, F.N.; Sherwin, S.J. Comparison of various fluid-structure interaction methods for deformable bodies. *Comput. Struct.* **2007**, *85*, 833–843. [[CrossRef](#)]
23. Wijesooriya, K.; Mohotti, D.; Amin, A.; Chauhan, K. Comparison between an uncoupled one-way and two-way fluid structure interaction simulation on a super-tall slender structure. *Eng. Struct.* **2021**, *229*, 111636. [[CrossRef](#)]
24. Bathe, K.J.; Zhang, H.; Ji, S. Finite element analysis of fluid flows fully coupled with structural interactions. *Comput. Struct.* **1999**, *72*, 1–16. [[CrossRef](#)]
25. Menter, F.R. Two-equation eddy-viscosity turbulence models for engineering applications. *AIAA J.* **1994**, *32*, 1598–1605. [[CrossRef](#)]
26. Morden, J.A.; Hemida, H.; Baker, C.J. Comparison of RANS and detached eddy simulation results to wind-tunnel data for the surface pressures upon a class 43 high-speed train. *J. Fluids Eng. Trans. ASME* **2015**, *137*, 041108. [[CrossRef](#)]
27. Li, X.; Krajnovic, S.; Zhou, D. Numerical Study of the Unsteady Aerodynamic Performance of Two Maglev Trains Passing Each Other in Open Air Using Different Turbulence Models. *Appl. Sci.* **2021**, *11*, 11894. [[CrossRef](#)]
28. Huo, S.; Huang, H.; Huang, D.; Liu, Z.; Chen, H. Modal characteristics and fluid–structure interaction vibration response of submerged impeller. *JVC/J. Vib. Control* **2022**, *28*, 2020–2031. [[CrossRef](#)]
29. Zhang, H.; Bathe, K.-J. Direct and iterative computing of fluid flows fully coupled with structures. *Comput. Fluid Solid Mech.* **2001**, *2001*, 1440–1443.
30. Chen, G.; Li, X.B.; Liu, Z.; Zhou, D.; Wang, Z.; Liang, X.F.; Krajnovic, S. Dynamic analysis of the effect of nose length on train aerodynamic performance. *J. Wind Eng. Ind. Aerodyn.* **2019**, *184*, 198–208. [[CrossRef](#)]
31. Dong, T.; Liang, X.; Krajnović, S.; Xiong, X.; Zhou, W. Effects of simplifying train bogies on surrounding flow and aerodynamic forces. *J. Wind Eng. Ind. Aerodyn.* **2019**, *191*, 170–182. [[CrossRef](#)]
32. Zhang, J.; Adamu, A.; Su, X.; Guo, Z.; Gao, G. Effect of simplifying bogie regions on aerodynamic performance of high-speed train. *J. Cent. South Univ.* **2022**, *29*, 1717–1734. [[CrossRef](#)]
33. Wang, S.; Bell, J.R.; Burton, D.; Herbst, A.H.; Sheridan, J.; Thompson, M.C. The performance of different turbulence models (URANS, SAS and DES) for predicting high-speed train slipstream. *J. Wind Eng. Ind. Aerodyn.* **2017**, *165*, 46–57. [[CrossRef](#)]
34. Siemens. *STAR-CCM + User Guide*; Version 16.06; Siemens: Munich Germany, 2021.
35. Gent, A.N. *Engineering with Rubber—How to Design Rubber Components*, 2nd ed.; Carl Hanser Verlag: Munich, Germany, 2001.

Disclaimer/Publisher’s Note: The statements, opinions and data contained in all publications are solely those of the individual author(s) and contributor(s) and not of MDPI and/or the editor(s). MDPI and/or the editor(s) disclaim responsibility for any injury to people or property resulting from any ideas, methods, instructions or products referred to in the content.